Nonadiabatic laser-induced alignment of iodobenzene molecules

Emmanuel Péronne,* Mikael D. Poulsen, and Henrik Stapelfeldt[†]

Department of Chemistry, University of Aarhus, 8000 Århus C, Denmark

Christer Z. Bisgaard

Department of Physics and Astronomy, University of Aarhus, 8000 Århus C, Denmark

Edward Hamilton and Tamar Seideman[‡]

Department of Chemistry, Northwestern University, 2145 Sheridan Road, Evanston, Illinois 60208-3113, USA

Nonadiabatic alignment of an asymmetric top molecule induced by a short, moderately intense laser pulse is studied theoretically and experimentally. Numerically, we solve nonperturbatively the time-dependent Schrödinger equation for a general asymmetric top molecule subject to a moderately intense laser field, and analyze the dependence of the alignment dynamics on the field strength and on the rotational temperature. Experimentally, we use time-resolved photofragment imaging to measure the time-dependent angular distributions of the spatial orientation of the molecules. Our studies, using iodobenzene as a test molecule, focus on the short-time alignment dynamics, during and after the pulse.

PACS number(s): 42.50.Hz, 33.80.−b, 33.15.Bh, 42.65.Re

I. INTRODUCTION

Spatial alignment of an anisotropic molecule can be induced by a moderately strong, polarized laser field due to the polarizability interaction between the field and the induced dipole moment [1]. For a linearly polarized field, the interaction creates a potential minimum at configurations where the molecular axis with the largest polarizability aligns with the polarization direction.

The alignment dynamics depends on the time scale of turn on and off of the laser field with respect to the natural rotational period(s) of the molecule [2–5]. For slow turn-on, characterizing studies with long laser pulses, the alignment occurs adiabatically. Each initial rotational eigenstate evolves into an aligned state that reaches the strongest degree of alignment at the peak of the pulse [5–9]. If the field is also turned off slowly, the alignment disappears concurrently and the molecule returns adiabatically to the original field-free state. Thus for adiabatic turn-on and -off the molecules are only aligned in the presence of the field.

Alternatively, the laser field can be turned on and off much faster than the rotational period(s) [2–5,10–17]. In this nonadiabatic case the field excites the molecule to a time-dependent superposition of field-free rotational eigenstates. The resulting rotational wave packet gives rise to transient alignment due to the dephasing and rephasing of its individual components. Consequently, short pulse alignment opens up the possibility for alignment after the pulse is turned off, i.e., under field-free conditions. This mode of alignment is of particular interest since it enables using aligned molecules without the possible disturbance from the strong alignment field.

Most studies have focused on linear molecules aligned by short linearly polarized laser pulses. Calculations showed that alignment can be achieved both shortly after the pulse and at much later times, periodically spaced by the rotational period [3,13]. Experimental evidence of nonadiabatic alignment was given by Rosca-Pruna and Vrakking [18,19] followed by a number of very recent studies [20–26].

The purpose of the present paper is to give a more thorough discussion of our studies of nonadiabatic alignment of asymmetric top molecules than what was presented in our recent paper [23]. In particular, we study both theoretically and experimentally rotational wave packets of asymmetric top molecules induced by a nonresonant alignment pulse. We demonstrate that it is possible to achieve field-free alignment and investigate quantitatively the role played by the field and system parameters in determining the degree and time evolution of the alignment. Iodobenzene is used as a model in the calculations and the experiments.

The second section of the paper is devoted to the theory of alignment of asymmetric top molecules by intense laser pulses, which we formulate within nonperturbative quantum mechanics. We provide only a brief discussion of the theory, to avoid repetition of material presented in Ref. [26], and hence Sec. II is not self-contained. In Sec. III we present the numerical results, the fourth section describes the experimental setup and the data analysis method, and in the fifth section we discuss the experimental results and compare them with the numerical results. The final section concludes this work with an outlook to future research and applications.

II. THEORY

We consider a general molecule subject to a moderately intense laser field, treating the field as a classical entity,

*Present address: Laboratoire des Milieux Désordonnés et Hétérogènes, Université Pierre et Marie Curie, 75252 Paris Cedex 05, France.

[†]Electronic address: henriks@chem.au.dk

[‡]Electronic address: seideman@chem.northwestern.edu

$$\boldsymbol{\epsilon}(t) = \boldsymbol{\varepsilon}(t)\cos(\omega t), \tag{1}$$

where $\boldsymbol{\varepsilon}(t) = \hat{\boldsymbol{\varepsilon}}\varepsilon(t)$, $\hat{\boldsymbol{\varepsilon}}$ is a unit vector in the field polarization direction, $\varepsilon(t)$ is the pulse envelope, and ω is the center frequency. In the far-off resonance limit, the field-matter interaction can be cast in the form of an induced Hamiltonian,

$$H_{\text{ind}} = -\frac{1}{4}\sum_{\rho,\rho'}\varepsilon_\rho \alpha_{\rho\rho'}\varepsilon_{\rho'}^* = -\sum_\rho \varepsilon_\rho \mu_\rho^{\text{ind}}, \quad \mu_\rho^{\text{ind}} = \frac{1}{4}\sum_{\rho'}\alpha_{\rho\rho'}\varepsilon_{\rho'}^*, \tag{2}$$

where $\rho, \rho' = x, y, z$ are the space-fixed coordinates, α is the molecular polarizability tensor, and $\boldsymbol{\mu}^{\text{ind}}$ defines an induced electric dipole vector. Equation (2) is derived from the standard electric dipole Hamiltonian through adiabatic elimination of all excited vibronic states in which real population does not reside in the course of the pulse [27]. It is thus limited to the case of a nonresonant laser field.

In the present work we restrict attention to the case of linearly polarized fields, $\hat{\boldsymbol{\varepsilon}} = \hat{\mathbf{z}}$, where we followed the standard convention of defining the space-fixed z axis as the field polarization vector. Transforming the polarizability tensor from the space- to the body-fixed frame (see Ref. [28], Table 1) we have

$$H_{\text{ind}} = -\frac{1}{4}\varepsilon^2(t)[\alpha^{ZX}\cos^2\theta + \alpha^{YX}\sin^2\theta\sin^2\chi], \tag{3}$$

where we introduced generalized polarizability anisotropies as $\alpha^{ZX} = \alpha_{ZZ} - \alpha_{XX}, \alpha^{YX} = \alpha_{YY} - \alpha_{XX}, \alpha_{kk}, k = X, Y, Z$ are the body-fixed components of the polarizability tensor, and $\hat{R} = (\theta, \phi, \chi)$ are the Euler angles of rotation specifying the orientation of the body with respect to the space-fixed frame. In Eq. (3) we omit a term independent of the angles that amounts to an overall shift of the potential and has no effect on the alignment dynamics. The dependence of the interaction on θ and χ—the polar Euler angle and the angle of rotation about the body-fixed Z axis—gives rise to the population of a broad wave packet in J and K spaces, J being the matter angular momentum and K its body-fixed Z projection. The independence of Eq. (3) on ϕ—the angle of rotation about the space-fixed z axis—leads to conservation of the magnetic quantum number M. In the symmetric top (or linear) rotor limit, $\alpha_{XX} = \alpha_{YY}$, Eq. (3) reduces to the familiar form,

$$H_{\text{ind}} = -\frac{1}{4}\varepsilon^2(t)\Delta\alpha\cos^2\theta, \quad \Delta\alpha = \alpha_\| - \alpha_\perp, \tag{4}$$

where $\alpha_\|$ and $\alpha_\perp$ are the components of the polarizability tensor parallel and perpendicular to the molecular symmetry axis, respectively. Equation (4) has been used in a large number of theoretical studies of the alignment dynamics of diatomic molecules during the past few years. With Eq. (3), the complete Hamiltonian takes the form

$$H = H_{\text{rot}} + H_{\text{ind}}, \tag{5}$$

where the field-free Hamiltonian is approximated in the rigid rotor limit by the rotational kinetic energy H_{rot}.

The time evolution during and after the laser pulse is determined nonperturbatively by expanding the wave packet in a complete set of stationary eigenstates, to convert the time-dependent Schrödinger equation into a set of first-order coupled differential equations. One convenient choice of a basis set is the set of symmetric top eigenstates,

$$|\Psi_i(t)\rangle = \sum_{JK} C_i^{JK}(t)|JKM\rangle, \tag{6}$$

where

$$\langle\hat{R}|JKM\rangle = \sqrt{\frac{2J+1}{8\pi^2}}D_{MK}^{J*}(\hat{R}), \tag{7}$$

$D_{mk}^j(\hat{R})$ are standard Wigner matrices and we use the notation of Zare [29]. The subscript i in Eq. (6) denotes the set of initial conditions and includes the energy level of the initial state and its magnetic quantum number (that is conserved in a linearly polarized field, $M = M_i$). Substituting Eq. (6) into the time-dependent Schrödinger equation and using the orthonormality of the basis functions we obtain a set of first-order coupled differential equations for the expansion coefficients,

$$i\dot{C}_i^{JK}(t) = \sum_{J'K'} C_i^{J'K'}(t)\{\langle JKM|H_{\text{rot}}|JK'M\rangle\delta_{J'J} + \langle JKM|H_{\text{ind}}|J'K'M\rangle\}. \tag{8}$$

The first term on the right-hand side of Eq. (8) consists of the rotational energy and the nonradiative (asymmetric top) coupling and conserves J as well as the parity of K. The second, radiative term is responsible for the excitation of a rotational wave packet and vanishes after turn-off of the laser pulse. Both the nonradiative and the radiative coupling terms are analytically expressible.

An alternative expansion in terms of the eigenfunctions of the field-free Hamiltonian H_{rot} yields a set similar to Eq. (8), where, however, the nonradiative matrix elements on the right-hand side reduce to the diagonal energy term. From a numerical view point the latter approach is clearly more efficient than Eq. (6) as it allows the field-free dynamics subsequent to turn-off of the pulse to be determined analytically. For the purpose of the discussion below, and for gaining insight into the features that underlie the time evolution, Eq. (6) is nevertheless more convenient.

With $\Psi_i(t)$ determined, all observables can be computed nonperturbatively. Of specific interest are the expectation values of J^2 and K^2,

$$\langle J^2\rangle_i(t) = \langle\Psi_i(t)|J(J+1)|\Psi_i(t)\rangle = \sum_{JK}|C_i^{JK}(t)|^2 J(J+1), \tag{9}$$

$$\langle K^2\rangle_i(t) = \langle\Psi_i(t)|K^2|\Psi_i(t)\rangle = \sum_{JK}|C_i^{JK}(t)|^2 K^2 \tag{10}$$

that characterize the degree and sense of rotational excitation, and the expectation values of $\cos^2\theta$ and $\cos^2\chi$,

$$\langle \cos^2\theta \rangle_i(t) = \sum_{JKJ'} C_i^{JK}(t) C_i^{J'K*}(t) \langle J'KM|\cos^2\theta|JKM\rangle,$$

$$(11)$$

$$\langle \cos^2\chi \rangle_i(t) = \sum_{JKK'} C_i^{JK}(t) C_i^{JK'*}(t) \langle JK'M|\cos^2\chi|JKM\rangle$$

$$(12)$$

that characterize the alignment dynamics. The expectation values of J^2 and $\cos^2\theta$ are often used to quantify the rotational excitation and associated alignment in linear rotors whereas $\langle K^2\rangle$ and $\langle\cos^2\chi\rangle$ are determined by both the radiative and the nonradiative interactions. As was illustrated in the linear rotor case [3,24], much more information is available from the complete angular distribution, $|\Psi(\theta,\chi;t)|^2$, where all moments are contained, than what is available from Eqs. (11) and (12). This is observed numerically and experimentally in the following sections.

Thermally averaged observables, $\langle O\rangle_T(t)$, are obtained from the corresponding $\langle O\rangle_i(t)$ of Eqs. (9)–(12) as

$$\langle O\rangle_T(t) = \frac{1}{Q}\sum_i w_i(T_{\rm rot})\langle O\rangle_i(t),\qquad(13)$$

where Q is the rotational partition function, $w_i(T_{\rm rot})$ is a Boltzmann weight function, and $T_{\rm rot}$ is the rotational temperature.

To gain better insight into the features underlying the alignment it is useful to express Eq. (3) in terms of rotation matrices as

$$H_{\rm ind} = -\frac{\varepsilon^2(t)}{4}\{\alpha_\parallel D_{00}^2(\hat{R}) + \alpha_\perp[D_{02}^2(\hat{R}) + D_{0-2}^2(\hat{R})]\}, \quad(14)$$

where $\alpha_\parallel = \frac{1}{3}(2\alpha_{ZZ}-\alpha_{XX}-\alpha_{YY})$ and $\alpha_\perp = (1/\sqrt{6})(\alpha_{XX}-\alpha_{YY})$ are polarizability anisotropies parallel and perpendicular to the Z axis, respectively, and an angle-independent term has been omitted. Together with Eq. (6) and the orthogonality properties of the rotation matrices,

$$\int d\hat{R}D_{m_1,k_1}^{j_1*}D_{m_2,k_2}^{j_2}D_{m_3,k_3}^{j_3} \propto \delta_{m_1,m_2+m_3}\delta_{k_1,k_2+k_3}, \quad(15)$$

Eq. (14) illustrates explicitly that the ϕ independence of Eq. (3) translates into conservation of M in a linearly polarized field. It also shows that $H_{\rm ind}$ conserves the parity of K (as does $H_{\rm rot}$) while mixing J levels of different parity. Using Eq. (14) in Eq. (11) we have

$$\langle \cos^2\theta\rangle(t) = \frac{2}{3}\sum_{JK}\left\{\left[\frac{1}{2} + \langle JKM|D_{00}^2|JKM\rangle\right]|C_i^{JK}|^2 \right.$$
$$+ 2\mathrm{Re}(C_i^{JK}C_i^{J-1K*})\langle J-1KM|D_{00}^2|JKM\rangle$$
$$\left. + 2\mathrm{Re}(C_i^{JK}C_i^{J-2K*})\langle J-2KM|D_{00}^2|JKM\rangle\right\}.$$

$$(16)$$

In Eq. (16), the first term in curly brackets is diagonal in J and remains constant after the pulse turn-off. The second and third terms reflect interference between levels with $J'=J\pm1$

and $J'=J\pm2$, respectively. The interferences between K levels, which the χ independence of the operator on the left-hand side of Eq. (16) eliminates, are contained in the $\langle\cos^2\chi\rangle$ of Eq. (12). In the latter equation, however, integration over the polar Euler angle θ cannot be carried out analytically. Equation (16) shows explicitly that in the $H_{\rm ind}\rightarrow0$ limit (where all terms in the curly bracket but the $1/2$ vanish) $\langle\cos^2\theta\rangle\rightarrow1/3$.

Of particular interest is the functional form of the polar angle dependence of the probability density, this function being directly measurable with our experimental technique. Using Eq. (6) and expressing the Wigner matrices in Eq. (7) in terms of reduced matrices as

$$D_{MK}^J(\hat{R}) = e^{-iM\phi}d_{MK}^J(\theta)e^{-iK\chi}\qquad(17)$$

we have

$$P(\theta,t) = \int d\chi d\phi|\Psi_i(\phi,\theta,\chi;t)|^2$$
$$= \sum_{JK}\left\{\frac{1}{2}\tilde{J}^2|C_i^{JK}(t)|^2[d_{MK}^J(\theta)]^2 \right.$$
$$\left. + \sum_{J'<J}\tilde{J}\tilde{J}'\,\mathrm{Re}[C_i^{JK}(t)C_i^{J'K*}(t)]d_{MK}^J(\theta)d_{MK}^{J'}(\theta)\right\},$$

$$(18)$$

where $\tilde{j} = \sqrt{2j+1}$.

III. NUMERICAL RESULTS

In this section we apply the theory of Sec. II to describe the alignment dynamics of iodobenzene under the conditions relevant to our experiment. We choose the body-fixed Z axis as the C-I bond (the a axis of iodobenzene) with the molecular plane defining the body-fixed YZ plane. With rotational constants $A=5680.21$ MHz, $B=747.88$ MHz, and $C=660.87$ MHz (obtained from electronic structure calculations), iodobenzene is a near prolate symmetric top, characterized by an asymmetry parameter $\kappa=(2B-A-C)/(A-C) =-0.964$ (where $\kappa=-1$ corresponds to the prolate symmetric top limit.) The polarizability tensor of iodobenzene has been calculated within linear-response theory, using a Hartree-Fock basis. We found the nonvanishing components of α to be $\alpha_{XX}=68.9, \alpha_{YY}=103.4$, and $\alpha_{ZZ}=145.3$ Bohr^3. Thus the polarizability tensor of iodobenzene, by contrast to its inertia tensor, is rather asymmetric.

Figures 1 and 2 illustrate the dynamics of rotational excitation and wave-packet alignment of iodobenzene during and after the laser pulse. Panels (a) and (b) in Fig. 1 show the expectation values of J^2 and K^2, and panel (c) provides the expectation value of $\cos^2\theta$. Whereas the expectation value of the total angular momentum squared is obviously conserved after the pulse turn-off, K is not a conserved quantum number in the asymmetric top system and hence $\langle K^2\rangle$ in Fig. 1(b) is not constant after the interaction. The variation in $\langle K^2\rangle$ under field-free conditions is a measure of the deviation from the symmetric top limit and is thus rather small in the present
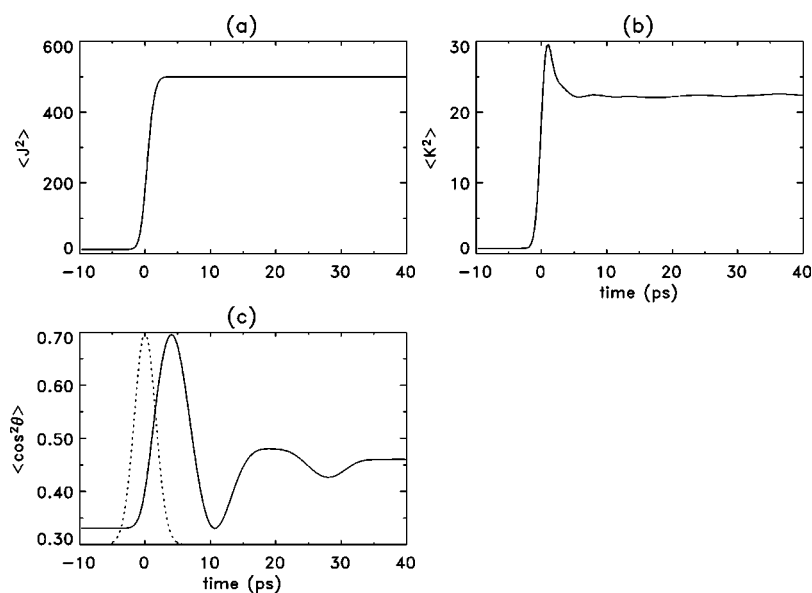
FIG. 1. Time evolution of the temperature-averaged dynamic observables of iodobenzene as described in the theory of Sec. II, for a 3.82-ps Gaussian alignment pulse with peak intensity 6×10^{11} W/cm^2, at a rotational temperature of 400 mK. (a) Expectation value of J^2. (b) Expectation value of K^2. (c) Expectation value of $\cos^2\theta$ (solid), with the alignment pulse shape (dashed) included for reference.

system. The magnitude of $\langle J^2 \rangle$ [Fig. 1(a)] is typical of polyatomic systems of the inertia range of iodobenzene, although remarkably large by comparison to the diatomic systems dealt with previously. The high degree of rotational excitation under moderate intensity (here 6×10^{11} W/cm^2) results from the large density of rotational states of this and similar systems. The shift of the alignment maximum with respect to the peak of the pulse (at time=10 ps), Fig. 1(c), is a general feature of the nonadiabatic domain and is well understood from previous studies of linear molecules [2,3]. For a fixed peak intensity the shift increases as the ratio of the pulse duration to the rotational periods decreases and the excitation approaches the impulse limit.

The expectation value of $\cos^2\theta$ in the wave packet has been used in most strong field alignment studies as a measure of the alignment and is useful as a comparison and quantification criterion. Nonetheless, it has been shown in theoretical work before [2,3,10] that the wave-packet probability distribution contains considerably more information

about the alignment dynamics than this average measure, since it is sensitive to all moments of the alignment. In Fig. 2 we show a contour plot of the probability density of the wave packet corresponding to Fig. 1, $P(\theta, t)$ $= \Sigma_i w_i(T_{rot}) \int d\chi d\phi |\Psi_i(\phi, \theta, \chi; t)|^2$ of Eq. (21), as a function of the polar Euler angle and time.

We remark that Figs. 1 and 2 are not intended to replicate any particular experimental conditions discussed in Sec. V, but are provided to show the relationship between the different measures of alignment. In particular, it is seen that the maximum value of the probability distribution (Fig. 2) occurs slightly earlier in time than the maximum in the expectation value of $\cos^2\theta$ [Fig. 1(c)], illustrating that the definition of the "alignment peak" depends on the observable. The same behavior is also observed experimentally, as discussed in Sec. V.

In the experiments considered here, the observable is averaged also over the inhomogeneous spatial intensity profile of the laser field since the detection is not spatially restricted to the center of the laser focus (see also Ref. [30]). To account for the spatially inhomogeneous intensity distribution we assume that the alignment and dissociation pulses are concentric ellipsoids of identical orientation, each with a two-dimensional Gaussian profile. The ratio of the spot sizes of the two fields $\omega^{\text{probe}}/\omega^{\text{alignment}} = \omega^{266}/\omega^{800} \approx 0.7$ is determined experimentally (see Sec. IV). With this ratio the averaging procedure over the sampled intensities is independent of the absolute dimensions, as it reduces to a normalized statistical distribution reflecting the overlap of the alignment and dissociation Gaussian intensity profiles.

Figure 3 shows the initial alignment peak over a range of four successive peak intensity values, for a 2.7-ps Gaussian alignment pulse. As the intensity increases, the initial alignment is enhanced, its maximum is shifted to earlier time, and its temporal profile becomes increasingly structured. All three effects result from the increased degree of rotational excitation with intensity. In the short pulse domain the increase of J from the thermal value is roughly the ratio of the pulse duration to the Rabi period [2,5], Ω_R^{-1}, with $\Omega_R \propto I$, and
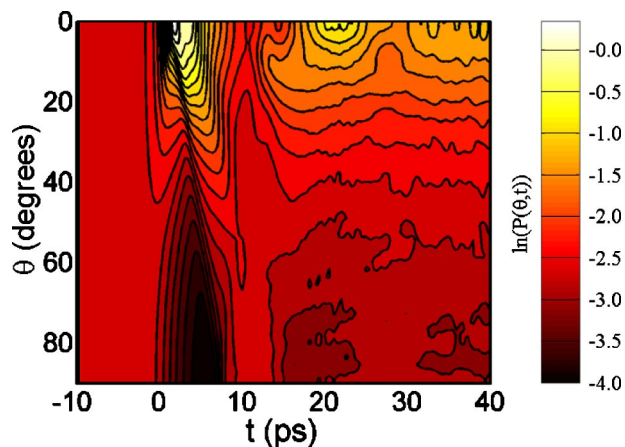

FIG. 2. (Color online) Contour plot of the thermally averaged probability distribution for iodobenzene as a function of time and the polar Euler angle. The temperature and pulse parameters are as in Fig. 1.
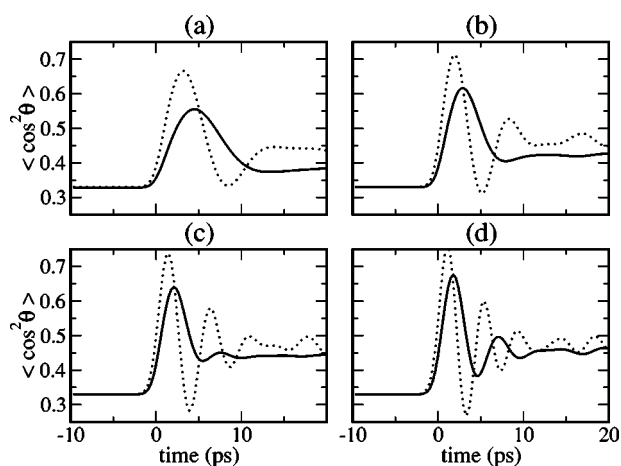
FIG. 3. Alignment dynamics of iodobenzene as a function of the focal averaged peak intensity (solid lines) at a temperature of 2.4 K. The corresponding dynamics without focal averaging is overlaid as a dotted line for each of the four panels. The peak intensities are (a) 1×10^{12} W/cm^2, (b) 2×10^{12} W/cm^2, (c) 3×10^{12} W/cm^2, (d) 4×10^{12} W/cm^2. The pulse duration is 2.7 ps.

hence the degree of rotational excitation (and with it the alignment) increases with the intensity and with the pulse duration. With increasing content of rotational level spacing in the wave packet, the beat pattern becomes richer and the frequency of oscillations increases. The rate of dephasing of the wave packet is proportional to $(\Delta J)^2$, ΔJ being the width of the wave packet in quantum number space, and thus increases sharply with intensity. The primary effect of the focal averaging, in addition to shifting the peak to a position that reflects the inclusion of lower intensities in the average, is to dampen the oscillations after the initial alignment peak.

The exact rotational temperature in the experiment is not measured here, making a direct comparison with the experimental data impossible. It is nevertheless useful to investigate the effect of temperature numerically, so as to explore its role in determining the observable. In Fig. 4 we show the temporal profile of the expectation value of $\cos^2\theta$ at three
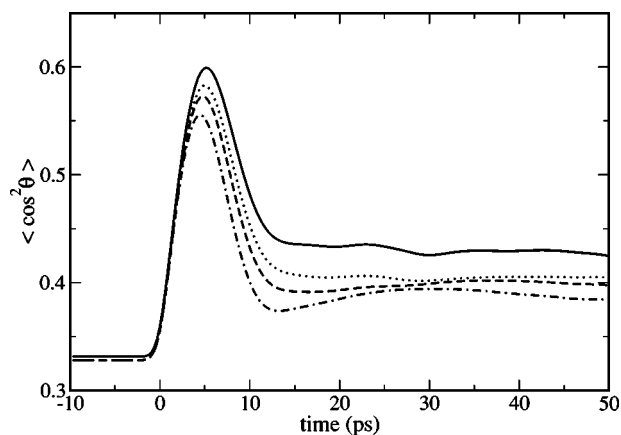

FIG. 4. Alignment dynamics of iodobenzene as a function of the rotational temperature at a focal averaged peak intensity of 1×10^{12} W/cm^2. Solid, 0 mK; dotted, 400 mK; dashed, 1.2 K; dot-dashed, 2.4 K.
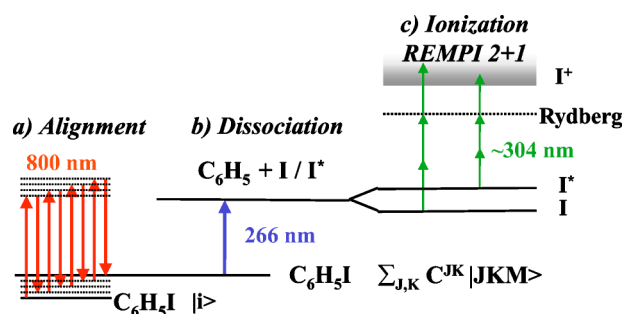

FIG. 5. (Color online) Principle of the experiment: (a) Excitation of an initial rotational state $|i\rangle$ of iodobenzene by an 800-nm pulse. (b) Dissociation of C$_6$H$_5$I following one-photon absorption from a 266-nm pulse. (c) Selective resonant $(2+1)$-photon ionization of the I or the I* photoproducts by a nanosecond laser pulse.

different temperatures, again for a 2.7-ps Gaussian alignment pulse. As the temperature increases, the alignment is gradually suppressed and its duration shortens. Nevertheless, temperature effects in the early time dynamics are minor. This stands in contrast to the dominant role of rotational temperature in the long time response, where the temporal shifts of the rotational revivals of wave packets resulting from different initial states in a thermal ensemble give rise to strong variation of the observable pattern as temperature increases.

IV. EXPERIMENTAL SETUP

The basic idea of the experiment is to induce nonadiabatic one-dimensional alignment of a sample of iodobenzene molecules and measure the spatial orientation of the C-I axis as a function of time. It is implemented in a three step procedure as illustrated in Fig. 5.

First, iodobenzene molecules are irradiated by a linearly polarized, 2–3 ps-long 800-nm pulse. This creates molecular alignment because each initially populated rotational state is excited to a rotational wave packet as a result of successive nonresonant Raman transitions [Fig. 5(a)] during the pulse. Second, the iodobenzene molecules are dissociated, through one-photon excitation, into an iodine and a phenyl radical by a 250-fs-long ultraviolet (266 nm) pulse [Fig. 5(b)]. The dissociation process is direct [31] so the iodine photofragments fly away in the direction of the symmetry axis of their parent molecule. The spatial orientation of the molecular C-I axis, at the time of the dissociation pulse, can therefore be measured by recording the direction of the photofragments. This is performed by two-dimensional (2D) ion imaging of the I$^+$ ions formed after resonant multiphoton ionization (REMPI) of either the I or the I* photofragments [Fig. 5(c)]. The ionization step does not change the velocity vector of the iodine atoms.

A schematic of the experimental setup is shown in Fig. 6. A pulsed molecular beam, formed by expanding 1 mbar iodobenzene in 1–4 bars of helium, is crossed at 90° by three laser beams. The alignment pulses are created by directing $\sim 550~\mu$J of the output from a 100-fs, 1-kHz Ti-sapphire laser through a pair of SF11 prisms. The resulting pulses are 2–3 ps long [full width at half maximum (FWHM)] with a
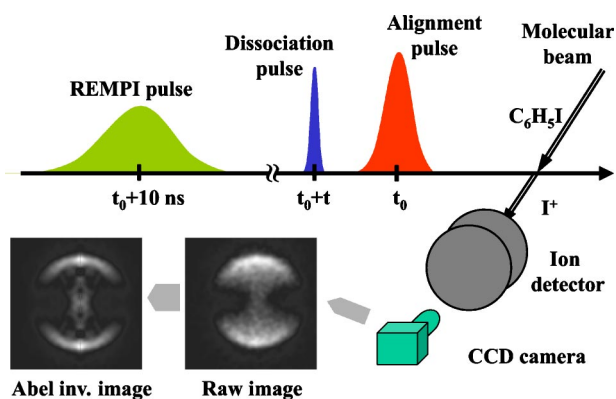
FIG. 6. Diagram of the experimental setup showing the molecular beam crossed at 90° by the three laser beams. The laser pulses are polarized vertically. The electrostatic lens imaging the I^+ ions onto the 2D detector is not displayed. The raw image to the right is recorded without the alignment pulse. It is the sum of 20 000 individual images (20 000 laser shots) and contains a total of 71.3×10^3 ion hits. The image to the left is the corresponding Abel inverted image represented as a slice through the 3D distribution.
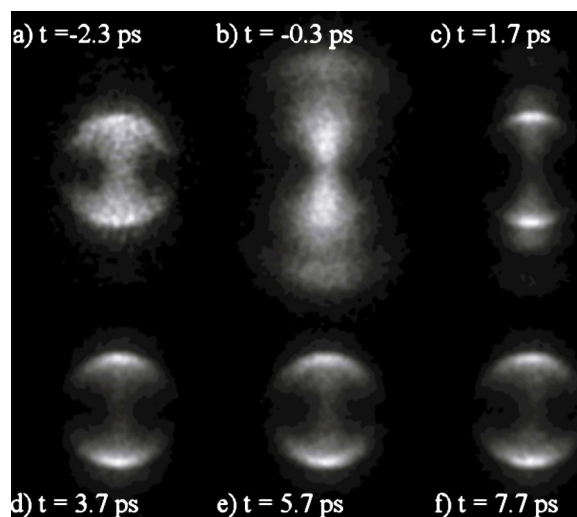

FIG. 7. Raw I^+ images recorded for six different delays between the alignment pulse and the dissociation pulse. The peak intensity of the alignment pulses is 3.4×10^{12} W/cm^2 and their duration is 2.2 ps (FWHM). The REMPI pulses are tuned to ionize the I* photofragments.

pulse energy $\leqslant 300$ μJ and they are focused to a spot size $\omega^{800} \sim 32$ μm. The dissociation pulses ($\lambda = 266$ nm), formed by third harmonic generation of ~ 250 μJ of the output from the Ti-sapphire laser in two BBO crystals, are delayed by t with respect to the alignment pulses. Their energy is $\sim 4–5$ μJ and the spot size ω^{266} is ~ 25 μm giving a peak intensity of $\sim 2 \times 10^{12}$ W/cm^2. The REMPI pulses are produced by second harmonic generation of the output of a YAG-pumped dye laser. Their pulse duration is ~ 5 ns, their spot size is $\omega^{304} \sim 25$ μm, their peak intensity is $\sim 1 \times 10^9$ W/cm^2, and they are delayed ~ 12 ns with respect to the alignment pulses. By tuning the wavelength of the REMPI pulses to 304.59 or 303.96 nm either ground-state iodine atoms I or spin excited iodine atoms I* are selectively detected [see Fig. 5(c)].

The iodine ions are accelerated by weak static electric fields, in a velocity map imaging setup [32], and detected by a 2D ion detector consisting of a microchannel plate (MCP) backed by a phosphor screen. The MCP is gated in a narrow time window (~ 0.6 μs) around the arrival time of the I^+ ions (~ 10.1 μs) ensuring that no other ions than those with a mass-to-charge ratio of I^+ are detected. The 2D ion images are recorded by a charge-coupled device camera. Each image is analyzed online such that the coordinates of the center of every ion hit is determined and stored. This procedure ensures subpixel resolution and minimizes the influence of any inhomogeneities across the detector surface. Typically, 5–15 ions are detected in each individual image and a total "raw" image is the sum of 20–30 000 individual images. An example of a raw image, recorded when only the dissociation and the REMPI pulses are used, is shown in Fig. 6. The wavelength of the REMPI laser is set to 303.96 nm such that the I* photofragments are recorded. Since the polarizations of the three laser beams are collinear and parallel to the plane of the detector any raw image recorded in the experiment can be Abel inverted and the 3D velocity distribution of the ions determined. Hereby, the angular distributions of the I^+ ions,

measured as a function of the angle between the polarization direction and the velocity vector of the I^+ ion, can be determined [34]. The Abel inverted image, obtained from the raw image, is also shown in Fig. 6 as a slice through the 3D distribution.

V. EXPERIMENTAL RESULTS

Figure 7 shows six raw ion images recorded with all three laser pulses present. The six images correspond to six different delays between the alignment and the dissociation pulses. When the molecules are dissociated prior to the alignment pulse [Fig. 7(a)], the image is similar to that recorded with only the dissociation and the REMPI pulses (Fig. 6) showing that no alignment has occurred yet. The localized angular distribution of the I^+ ions is the result of a nearly parallel one photon transition from the electronic ground state of iodobenzene to an excited repulsive state, followed by prompt dissociation into C_6H_5 and I* [31].

When the molecules are dissociated at the peak of the alignment pulse the ion image becomes more angularly confined along the polarization direction [Fig. 7(b)]. In addition, I^+ ions at both large radial distances, corresponding to large kinetic energies, and near the center, corresponding to low kinetic energies, are observed. These extra low and high kinetic energy ions are only observed when there is temporal overlap between the dissociation and the alignment pulse. The precise ionization mechanism was not investigated in detail but it is likely that formation of an electronically excited state by the dissociation pulse followed by rapid multiphoton ionization due to the strong alignment pulse plays a major role.

The angular confinement of the ions becomes more pronounced at $t = 1.7$ ps [Fig. 7(c)], which we interpret as alignment of the C-I axis along the laser polarization. At this time
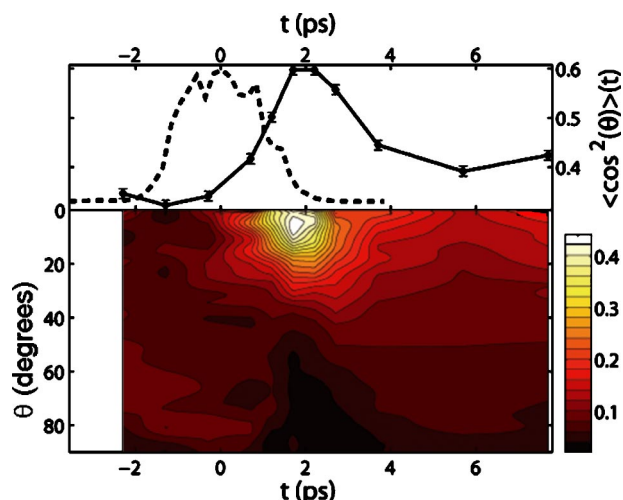
FIG. 8. (Color online) Lower part: Angular distribution of the molecular orientation, $f(\theta,t)$, measured at 11 different times with respect to a 2.2-ps-long alignment pulse (same as in Fig. 7). Upper part: $\langle\cos^2\theta\rangle$ (filled circles connected by lines) calculated directly from the measured angular distributions. The cross correlation between the alignment and the dissociation pulse is shown as the dashed curve.

the intensity of the alignment pulse is much reduced (to approximately one-tenth of the peak value), as can be seen directly in the image by the near complete disappearance of the extra low and high kinetic energy ions. At longer times the angular distribution first broadens [Fig. 7(d)], reaches a local maximum around $t=5.7$ ps [Fig. 7(e)] and finally narrows somewhat at $t=7.7$ ps [Fig. 7(f)].

Figure 8 provides a compact representation of $f(\theta,t)$, corresponding to the images shown in Fig. 7. The angular distributions measured are symmetric around $\theta=90°$, as expected, so they are only displayed for $0°\leqslant\theta\leqslant90°$. The figure also shows the expectation value of $\cos^2\theta$, determined directly from the measured $f(\theta,t)$ as $\langle\cos^2\theta\rangle(t)=\int f(\theta,t)\cos^2\theta\sin\theta d\theta$. Just before the alignment pulse ($t=-2.3$ ps) the distribution is essentially uniform, corresponding to randomly oriented molecules with $\langle\cos^2\theta\rangle=\frac{1}{3}$. During and shortly after the pulse the angular distribution gradually localizes around $\theta=0$. The most pronounced angular confinement around $\theta=0$ is reached at $t\sim1.8$ ps, whereas $\langle\cos^2\theta\rangle$ reaches its peak value of ~0.59 slightly later, at ~2.1 ps. The earlier appearance of the alignment maximum in the angular distribution compared to the $\langle\cos^2\theta\rangle$ time trace is in agreement with our numerical results [see Figs. 1(c) and 2]. Our experimental results stress the conclusion attained numerically in Sec. III that angular distributions at different times provide a more complete information of the alignment dynamics than $\langle\cos^2\theta\rangle(t)$ [3,24].

At larger delays, the localization of the angular distribution disappears rapidly and, correspondingly, the value of $\langle\cos^2\theta\rangle$ decreases towards a local minimum of ~0.37 at $t=5.7$ ps. At even longer times, $t=7.7$ ps, we observe a weak relocalization of the angular distribution around $\theta=0$. In similar measurements, where angular distributions were recorded out to larger times, we observed that the degree of alignment exhibits a damped oscillatory behavior until approximately $t=20$ ps. Hereafter the angular distribution remains constant but not uniform. The deviation from a uniform distribution is caused by the fact that the rotational wave packet, formed by the alignment pulse, forces the C_2 axis of the molecules to rotate with an angular momentum preferentially perpendicular to the polarization direction [19,26]. This permanent alignment results in a $\langle\cos^2\theta\rangle$ value between $\frac{1}{3}$ and $\frac{1}{2}$ depending on the initial rotational temperaure, the peak intensity, and the alignment pulse duration. Using alignment pulses with a duration of 2–3 ps and peak intensity $2–3.5\times10^{12}$ W/cm^2 we observed $\langle\cos^2\theta\rangle$ in the range 0.40–0.44.

We note that our experimental method of measuring the molecular orientation after the alignment pulse is turned off misses those molecules that undergo direct ionization by the dissociation pulse. These molecules originate primarily from the central part of the laser foci where the intensity is highest. Since this is also the region where the strongest alignment occurs and since ionization is most efficient for molecules with $\theta=0$, a fraction of the best aligned molecules are not included in the orientational measurement. As a consequence we expect that our measurement slightly underestimates the degree of alignment. This underestimate is likely more pronounced for measurements in the presence of the 800-nm alignment pulse, i.e., at times around zero, because the presence of both the alignment and the dissociation pulse causes much larger ionization than the dissociation pulse by itself [see Fig. 7(b)]. Therefore we expect that the measured degrees of alignment, shown in Fig. 8, for the range $-2<t<2$ ps are too small.

To illustrate the effect of the alignment pulse intensity on the alignment dynamics we measured the time-dependent angular distributions for two different intensities and the same pulse duration (FWHM ~2.7 ps). The results are shown in Fig. 9 along with the corresponding $\langle\cos^2\theta\rangle$ [35]. These results agree well with our numerical results with respect to the shape and positions of the initial alignment peak. The plot in the left panel of Fig. 9, with an intensity halfway between that of panels (a) and (b) in Fig. 3, is centered approximately at 4 ps, about midway between the maximum at 4.5 ps in Fig. 3(a) and the maximum at 2.9 ps in (b). The FWHM is
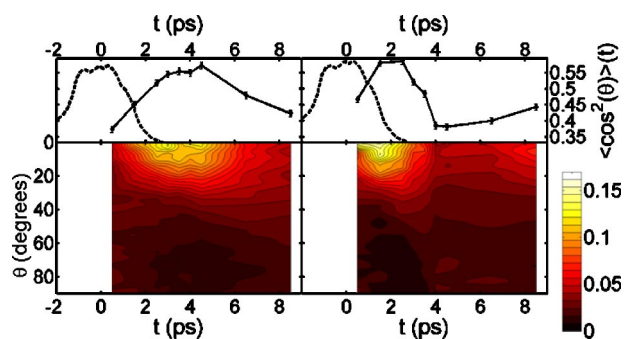
FIG. 9. (Color online) Alignment dynamics of iodobenzene induced by a 2.7-ps-long pulse at two different peak intensities. Left panel, 1.5×10^{12} W/cm^2; right panel, 4.1×10^{12} W/cm^2. The upper row shows $\langle \cos^2\theta \rangle$ vs time and the alignment pulse shape (arbitrary units). The lower row shows the measured angular distributions.

approximately 5 ps, again about midway between the values of 6 ps for (a) and 4 ps for (b). The right panel of Fig. 9, with a peak intensity close to (d) of Fig. 3, is centered approximately at 2 ps, as expected from the numerical prediction 1.8 ps in (d). The first minimum in the experiment, at about 4 ps, is slightly earlier than the minimum at 4.4 ps in panel (c), but much broader. The FWHM is narrowed to a little more than 3 ps, essentially identical to the numerical prediction of 2.5 ps. The discrepancy between the measured and numerical results regarding the magnitude of the alignment peaks arises from the higher rotational temperature in the experiments.

The effect of the rotational temperature has been investigated also experimentally. The rotational temperature is controlled by the backing pressure of helium in the supersonic expansion. In particular, seeding iodobenzene in 3-bar He produces a lower rotational temperature than using a backing pressure of 1 bar [34]. The degree of alignment shortly after the pulse for 1- and 3-bar He backing pressure is shown in Fig. 10. The experiments were carried out for two different alignment pulse shapes: In Fig. 10(a) the pulse duration is ~2.1 ps (FWHM) and the peak intensity I_0 is ~3.4 $\times 10^{12}$ W/cm^2 and in Fig. 10(b) the pulse duration is
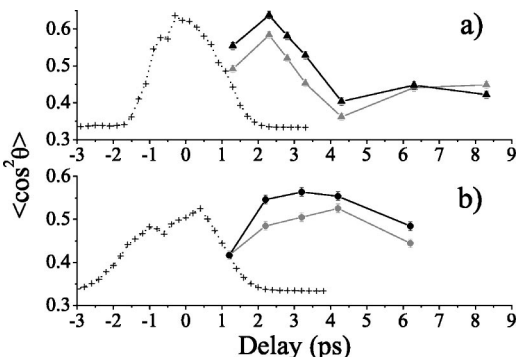

FIG. 10. Time dependence of $\langle \cos^2\theta \rangle$ for two different rotational temperatures of the molecular beam (black markers, C$_6$H$_5$I seeded in 3-bar He; gray markers, C$_6$H$_5$I seeded in 1-bar He) and for two different alignment pulse shapes: (a) peak intensity is 3.4 $\times 10^{12}$ W/cm^2 (triangles); (b) peak intensity is 1.0×10^{12} W/cm^2 (filled circles). The shape of the alignment pulse is shown by the dotted curve.

~2.9 ps (FWHM) and the peak intensity is ~1.0 $\times 10^{12}$ W/cm^2.

In both cases the degree of alignment is largest when the iodobenzene molecules have the lowest rotational temperature (3-bar He). The decrease in alignment at higher temperatures is consistent with the prediction of our theory—see Fig. 4. Without an absolute measurement of the temperature associated with each backing pressure, we are not able to make a more quantitative comparison at the present time. Note also that the first minimum becomes deeper and better resolved as the temperature increases, which may account for the discrepancies observed above in the results at high intensity.

VI. CONCLUSION

Using a combination of quantum dynamical theory and time-resolved photofragment imaging we studied the alignment dynamics of an asymmetric top molecule after exposure to a moderately intense few-picosecond-long laser pulse. The alignment dynamics, characterized by the angular distribution of molecular orientation and by the expectation value of $\langle \cos^2\theta \rangle$, was computed and measured at different intensities and for different rotational temperatures. We observed, numerically and experimentally, that the alignment reaches a maximum after the laser pulse, under field free conditions. The time delay between the pulse and the alignment maxima, as well as the temporal duration of the alignment prior to dephasing is controllable through choice of the pulse duration and intensity.

At much longer times (hundreds of picoseconds) we find strong enhancement of the degree of alignment in narrow (few ps) time windows [26]. These alignment transients correspond to revivals of the rotational wave packet. In recent work on the revival structure of complex polyatomics we showed, experimentally and numerically, that for asymmetric top molecules the alignment at the revivals is never as strong as the short time alignment that follows the pulse, because the complex rotational spectra of asymmetric tops prevents a complete reconstruction of the initial aligned state at the revivals. For asymmetric top molecules the early alignment maximum is thus of special interest as it is the global alignment maximum.

Our results illustrate that the alignment dynamics of asymmetric top molecules is significantly more complex than that of linear rotors. At the same time, they suggest that the vast controllability of the evolving alignment of molecules through various shapes and combinations of laser pulses, already demonstrated for linear molecules [14–16,36–38], will extend to the much richer realm of asymmetric top molecules.

Clearly, much remains to be accomplished on the alignment dynamics of polyatomic molecules, experimentally as well as theoretically and numerically. For applications of aligned molecules it is of interest to explore the utility of multiple pulses and of pulse shaping techniques as a route to improving the degree of field-free alignment. The majority of

applications of aligned polyatomics [1] will require three-dimensional rather than one-dimensional alignment. Using elliptically polarized pulses three-dimensional alignment has already been demonstrated in the adiabatic regime [39]. Schemes to achieve field-free three-dimensional alignment based on either short elliptically polarized pulses or pairs of orthogonally polarized linearly polarized pulses [40] are currently being explored.

[1] H. Stapelfeldt and T. Seideman, Rev. Mod. Phys. **75**, 543 (2003).

[2] T. Seideman, J. Chem. Phys. **103**, 7887 (1995).

[3] T. Seideman, Phys. Rev. Lett. **83**, 4971 (1999).

[4] J. Ortigoso, M. Rodriguez, M. Gupta, and B. Friedrich, J. Chem. Phys. **110**, 3870 (1999).

[5] T. Seideman, J. Chem. Phys. **115**, 5965 (2001).

[6] B. Friedrich and D. R. Herschbach, J. Phys. Chem. **99**, 15 686 (1995).

[7] W. Kim and P. M. Felker, J. Chem. Phys. **104**, 1147 (1996).

[8] H. Sakai, C. P. Safvan, J. J. Larsen, K. M. Hilligsøe, K. Hald, and H. Stapelfeldt, J. Chem. Phys. **110**, 10 235 (1999).

[9] J. J. Larsen, H. Sakai, C. P. Safvan, I. Wendt-Larsen, and H. Stapelfeldt, J. Chem. Phys. **111**, 7774 (1999).

[10] C. M. Dion, A. Keller, O. Atabek, and A. D. Bandrauk, Phys. Rev. A **59**, 1382 (1999).

[11] N. E. Henriksen, Chem. Phys. Lett. **312**, 196 (1999).

[12] M. Machholm, J. Chem. Phys. **115**, 10 724 (2001).

[13] I. Sh. Averbukh and R. Arvieu, Phys. Rev. Lett. **87**, 163601 (2001).

[14] A. Auger, A. Ben Haj-Yedder, E. Cances, C. Le Bris, C. M. Dion, A. Keller, and O. Atabek, Math. Methods Appl. Sci. **12**, 1281 (2002).

[15] C. M. Dion, A. Ben Haj-Yedder, E. Cances, C. Le Bris, A. Keller, and O. Atabek, Phys. Rev. A **65**, 063408 (2002).

[16] M. Leibscher, I. Sh. Averbukh, and H. Rabitz, Phys. Rev. Lett. **90**, 213001 (2003).

[17] G. Granucci, M. Persico, and P. Van Leuven, J. Chem. Phys. **120**, 7438 (2004).

[18] F. Rosca-Pruna and M. J. J. Vrakking, Phys. Rev. Lett. **87**, 153902 (2001).

[19] F. Rosca-Pruna and M. J. J. Vrakking, J. Chem. Phys. **116**, 6567 (2002); **116**, 6579 (2002).

[20] V. Renard, M. Renard, S. Guérin, Y. T. Pashayan, B. Lavorel, O. Faucher, and H. R. Jauslin, Phys. Rev. Lett. **90**, 153601 (2003).

[21] I. V. Litvinyuk, K. F. Lee, P. W. Dooley, D. M. Rayner, D. M. Villeneuve, and P. B. Corkum, Phys. Rev. Lett. **90**, 233003 (2003).

[22] J. G. Underwood, M. Spanner, M. Yu Ivanov, J. Mottershead, B. J. Sussman, and A. Stolow, Phys. Rev. Lett. **90**, 223001 (2003).

[23] E. Péronne, M. D. Poulsen, C. Z. Bisgaard, H. Stapelfeldt, and T. Seideman, Phys. Rev. Lett. **91**, 043003 (2003).

[24] P. W. Dooley, I. V. Litvinyuk, K. F. Lee, D. M. Rayner, M. Spanner, D. M. Villeneuve, and P. B. Corkum, Phys. Rev. A **68**, 023406 (2003).

[25] C. Z. Bisgaard, M. D. Poulsen, E. Péronne, S. S. Viftrup, and H. Stapelfeldt, Phys. Rev. Lett. **92**, 173004 (2004).

[26] M. D. Poulsen, E. Péronne, H. Stapelfeldt, C. Z. Bisgaard, S. S. Viftrup, E. Hamilton, and T. Seideman, J. Chem. Phys. **121**, 783 (2004).

[27] T. Seideman J. Chem. Phys. **111**, 4397 (1999).

[28] T. Seideman, Chem. Phys. Lett. **253**, 279 (1996).

[29] R. N. Zare, *Angular Momentum* (Wiley, New York , 1988).

[30] J. H. Posthumus, Rep. Prog. Phys. **67**, 623 (2004).

[31] J. E. Freitas, H. J. Hwang, and M. A. El-Sayed, J. Phys. Chem. **97**, 12 481 (1993).

[32] A. T. J. B. Eppink and D. H. Parker, Rev. Sci. Instrum. **68**, 3477 (1997).

[33] The intensity of the REMPI pulse is kept so low that it produces no I^+ ions by itself.

[34] M. D. Poulsen, E. Skovsen, and H. Stapelfeldt, J. Chem. Phys. **117**, 2097 (2002).

[35] The calculated and measured $\langle \cos^2 \theta \rangle$ was already reported in our previous paper on nonadiabatic alignment of iodobenzene—see Ref. [23].

[36] K. F. Lee, I. V. Litvinyuk, P. W. Dooley, M. Spanner, D. M. Villeneuve, and P. B. Corkum, J. Phys. B **37**, L43 (2004).

[37] M. Renard, E. Hertz, B. Lavorel, and O. Faucher, Phys. Rev. A **69**, 043401 (2004).

[38] D. Sugny, A. Keller, O. Atabek, D. Daems, C. M. Dion, S. Guerin, and H. R. Jauslin, Phys. Rev. A **69**, 033402 (2004).

[39] J. J. Larsen, K. Hald, N. Bjerre, H. Stapelfeldt, and T. Seideman, Phys. Rev. Lett. **85**, 2470 (2000).

[40] A. Stolow and J. G. Underwood (private communication).